

---

# GAUSSIAN PROCESS FOR TOMOGRAPHY

---

A PREPRINT

**Agnimitra Dasgupta**

Sonny Astani Department of Civil & Environmental Engineering  
University of Southern California  
Los Angeles, CA, USA  
adasgupt@usc.edu

**Carlo Graziani**

Mathematics and Computer Science Division  
Argonne National Laboratory  
Lemont, IL, USA  
cgraziani@anl.gov

**Zichao Wendy Di**

Mathematics and Computer Science Division  
Argonne National Laboratory  
Lemont, IL, USA  
wendydi@anl.gov

March 1, 2025

## ABSTRACT

Tomographic reconstruction, despite its revolutionary impact on a wide range of applications, suffers from its ill-posed nature in that there is no unique solution because of limited and noisy measurements. Traditional optimization-based reconstruction relies on regularization to address this issue; however, it faces its own challenge because the type of regularizer and choice of regularization parameter are a critical but difficult decision. Moreover, traditional reconstruction yields point estimates for the reconstruction with no further indication of the quality of the solution. In this work we address these challenges by exploring Gaussian processes (GPs). Our proposed GP approach yields not only the reconstructed object through the posterior mean but also a quantification of the solution uncertainties through the posterior covariance. Furthermore, we explore the flexibility of the GP framework to provide a robust model of the information across various length scales in the object, as well as the complex noise in the measurements. We illustrate the proposed approach on both synthetic and real tomography images and show its unique capability of uncertainty quantification in the presence of various types of noise, as well as reconstruction comparison with existing methods.

**Keywords** Gaussian process · Inverse problems · Tomographic reconstruction

## 1 Introduction

Tomographic imaging refers to the reconstruction of a 3D object from its 2D projections by sectioning the object, through the use of any kind of penetrating wave, from many different directions. It has had a revolutionary impact in a number of fields ranging from biology, physics, and chemistry to astronomy [1, 2]. The technique requires an accurate image reconstruction, however, and the resulting reconstruction problem is an ill-posed optimization problem because of insufficient measurements [3]. A direct consequence of ill-posedness is that the reconstruction does not have a unique solution. Therefore, quantifying the solution quality is challenging, given the absence of ground truth and the presence of measurement noise. Moreover, ill-posedness creates a requirement for regularization that imports new parameters to the problem. Regularization parameter choice can lead to substantial variations in reconstruction, and ascertaining optimal values of such parameters is difficult without availing oneself of ground truth [4].

The transition from an optimization perspective on tomographic inversion to a Bayesian statistical perspective can provide a useful reframing of these issues. In particular, the ill-posedness of the optimization view can be replaced by quantified uncertainty in the statistical view, whereas regularization now appears in the guise of parameter estimation.

A natural loss function also becomes available—the likelihood function—that can be used to tune parameters without knowledge of ground truth, based only on data fit.

A valuable setting for such a perspective is *Gaussian process* (GP) modeling [5]. A GP approach to tomography establishes a prior model over the object to be reconstructed comprising a *covariance function*, controlled by parameters that take over the role of regularization parameters, some of which establish a length scale (or possibly multiple length scales) relevant to the reconstruction. The predictions of the model at the detector are compared with observational data, where Gaussian noise—whether homoskedastic or heteroskedastic, or even correlated—can be naturally incorporated as part of the model, on the way to computing the likelihood function. The likelihood can then be maximized with respect to covariance parameters, providing the data fit approach to regularization. The resulting model reconstruction is obtained in the form of a predictive (“trained”) mean, attended by an estimated uncertainty encoded in the predictive (“trained”) covariance. Thus, ill-posedness is rephrased as uncertainty—measured by posterior predictive variance—and growth of measurement noise results in commensurate growth in posterior predictive variance, leading to “soft” rather than “hard” failure of the inversion, and a built-in quantification of reconstruction uncertainty.

The tomographic application is only one example of a much broader set of applications to which the same methodology may be adapted without much effort. Any inverse problem with a linear transfer function connecting the model space to the measurement space is amenable to a GP treatment that follows the lines described in this article. Examples include denoising, deblurring, Fourier transform of scattered data, and data assimilation for linear models [6, 7].

GP reconstruction has been previously applied to various tomographic settings. Svensson et al. [8] applied GP to soft x-ray tomography to reconstruct emissivity in stellarator plasmas. In order to capture length scale variations, continuously varying GP kernel length scales were implemented by using a Gibbs kernel with a local length-scale function set from the mean function of a second GP, in turn parameterized by values to be estimated at chosen “support points.” The resulting model has a large number of parameters, most of which provide for modulation of local length scales. The model assumes i.i.d. (that is, homoskedastic) measurement noise. Purisha et al. [9] demonstrated GP reconstruction in a continuous tomographic setting. Their approach is to implement covariance kernels using a truncated spectral representation, with basis functions that are amenable to closed-form implementation of the Radon transform, assuming no scale mixing, and a homoskedastic measurement noise model.

In this article we extend previous work in two main ways. First we examine the effect of various noise models, including heteroskedastic (i.e., non-i.i.d) measurement noise, a common experimental circumstance, and also examine the effect on reconstruction accuracy of using a measurement noise model that does not match the actual noise. Second we explore the use of kernel mixtures to flexibly model length-scale mixing in object reconstruction while avoiding proliferation of parameters.

For simplicity, we confine ourselves to reconstructing 2D images. Extension to the 3D case with a parallel beam is straightforward.

## 2 Method

Consider the physical domain  $\Omega \subseteq \mathbb{R}^2$  and the compactly supported function  $f : \Omega \rightarrow \mathbb{R}$ . The function  $f$  represents the physical property of the object one is interested in recovering (e.g., the attenuation coefficient in absorption imaging or elemental density in emission imaging). In practice, we cannot recover the desired object property at all points in space. Instead, we discretize  $\Omega$  (containing the compact object) into  $n \times n$  pixels, where the set of coordinates of each pixel center is  $\mathbf{X} = [\mathbf{x}_i] \in \mathbb{R}^{n^2}$ ,  $\mathbf{x}_i \in \Omega$ . The vectorized object (following lexicographical order) to be recovered is denoted as  $\mathbf{f} = [\mathbf{f}_i] \in \mathbb{R}^{n^2}$ , where  $\mathbf{f}_i = f(\mathbf{x}_i)$ . We impose a GP model on  $f(\cdot)$  by introducing a mean function  $m(\cdot)$  and a covariance function  $k(\cdot, \cdot)$ . These functions are parameterized by external parameters controlling features such as length scales, range of variability, and smoothness, as we will show below. Therefore, the GP model gives rise to a multivariate normal prior distribution on  $\mathbf{f}$ ,  $\mathbf{f} \sim \mathcal{N}(\mathbf{m}, \mathbf{K})$ , where the prior mean vector  $\mathbf{m} = [\mathbf{m}_i] \in \mathbb{R}^{n^2}$  and the prior covariance matrix  $\mathbf{K} = [\mathbf{K}_{ij}] \in \mathbb{R}^{n^2 \times n^2}$ .

For the experimental configuration, we index a beamlet by  $\tau$  and an angle by  $\theta$ , the collection of values of  $\tau$  by  $\mathcal{T}$ , and the collection of values of  $\theta$  by  $\Theta$ ; accordingly,  $N_\tau = |\mathcal{T}|$  is the number of beamlets, and  $N_\theta = |\Theta|$  is the number of angles. During the tomographic process, the object is rotated by  $N_\theta$  angles, where at each angle it is raster scanned with  $N_\tau$  steps [3].

We denote the set of measurements (i.e., the “sinogram”) by  $\mathbf{y} = [\mathbf{y}_t] \in \mathbb{R}^m$ , where  $m = N_\theta N_\tau$ . The forward model is governed by the discrete Radon transform [10], as follows:

$$\mathbf{y} = \mathbf{A}\mathbf{f} + \epsilon, \quad (1)$$

where  $\mathbf{A} = [\mathbf{A}_{t,i}] \in \mathbb{R}^{m \times n^2}$  and  $\mathbf{A}_{t,i}$  is the intersection length<sup>1</sup> of the  $t = \theta + (\tau - 1)N_\theta$  beam with the  $i$ th pixel. The measurement error  $\epsilon$  is assumed to be a zero-mean multivariate normal random variable with covariance  $\mathbb{E}[\epsilon\epsilon^T] = \Sigma_\epsilon$ .<sup>2</sup> In general,  $\epsilon$  is assumed to be statistically independent of the random variable  $\mathbf{f}$ , but it can be heteroskedastic or even correlated (i.e.,  $\Sigma_\epsilon$  may have nonzero off-diagonal entries.) For simplicity, we consider only the uncorrelated case in this work, with particular focus on both the homoskedastic (i.e.,  $\Sigma_\epsilon = \sigma_\epsilon^2 \mathbf{I}$ ) and the heteroskedastic noise (i.e., the diagonal elements of  $\Sigma_\epsilon$  may differ from each other).

Since  $\mathbf{f}$  is a normal random variable and  $\mathbf{y}$  is linearly dependent on  $\mathbf{f}$ , the pair  $[\mathbf{y}, \mathbf{f}]$  is necessarily governed by a normal distribution. Given that  $\mathbb{E}[\mathbf{f}] = \mathbf{m}$ ,  $\mathbb{E}[\mathbf{y}] = \mathbf{A}\mathbb{E}[\mathbf{f}] = \mathbf{A}\mathbf{m}$ ,  $\mathbb{E}[(\mathbf{f} - \mathbf{m})(\mathbf{f} - \mathbf{m})^T] = \mathbf{K}$ , and the statistical independence of  $\mathbf{f}$  and  $\epsilon$  (i.e.,  $\mathbb{E}[\mathbf{f}\epsilon^T] = 0$ ), we can obtain

$$\begin{aligned}\mathbb{E}[(\mathbf{y} - \mathbf{A}\mathbf{m})(\mathbf{f} - \mathbf{m})^T] &= \mathbf{A}\mathbb{E}[(\mathbf{f} - \mathbf{m})(\mathbf{f} - \mathbf{m})^T] = \mathbf{A}\mathbf{K}, \quad \text{and} \\ \mathbb{E}[(\mathbf{y} - \mathbf{A}\mathbf{m})(\mathbf{y} - \mathbf{A}\mathbf{m})^T] &= \mathbf{A}\mathbf{K}\mathbf{A}^T + \Sigma_\epsilon.\end{aligned}$$

Hence we have the joint normal distribution

$$\begin{Bmatrix} \mathbf{y} \\ \mathbf{f} \end{Bmatrix} \sim \mathcal{N}\left(\begin{Bmatrix} \mathbf{A}\mathbf{m} \\ \mathbf{m} \end{Bmatrix}, \begin{bmatrix} \mathbf{A}\mathbf{K}\mathbf{A}^T + \Sigma_\epsilon & \mathbf{A}\mathbf{K} \\ \mathbf{K}\mathbf{A}^T & \mathbf{K} \end{bmatrix}\right). \quad (2)$$

A simple choice for the GP prior mean function is a constant function; that is,  $m(\mathbf{x}) = c, \forall \mathbf{x} \in \Omega$ . We then have  $\mathbf{m} = c\mathbf{1}$ , where  $\mathbf{1}$  is a vector of all ones and  $c$  is a hyperparameter. An observation of the sinogram  $\mathbf{y}$  then yields the predictive distribution [5] as

$$\mathbf{f}|\mathbf{y} \sim \mathcal{N}(\mathbf{m}^*, \mathbf{K}^*),$$

where  $\mathbf{m}^*$  and  $\mathbf{K}^*$  are the predictive mean vector and covariance matrix, respectively, as

$$\begin{aligned}\mathbf{m}^* &= \mathbf{m} + \mathbf{K}\mathbf{A}^T[\mathbf{A}\mathbf{K}\mathbf{A}^T + \Sigma_\epsilon]^{-1}(\mathbf{y} - \mathbf{A}\mathbf{m}), \\ \mathbf{K}^* &= \mathbf{K} - \mathbf{K}\mathbf{A}^T[\mathbf{A}\mathbf{K}\mathbf{A}^T + \Sigma_\epsilon]^{-1}\mathbf{A}\mathbf{K}.\end{aligned}$$

Furthermore, we quantify the pixel-wise dispersion of the posterior  $\mathbf{f}|\mathbf{y}$  using the relative standard deviation (RSD), which is defined for the  $i$ th pixel as

$$\text{RSD}_i = \frac{\sqrt{\mathbf{K}_{ii}^*}}{|\mathbf{m}_i^*| + \varepsilon},$$

and  $\varepsilon$  ensures that  $\text{RSD}_i < \infty$  when  $\mathbf{m}_i^* = 0$ . Therefore, for a given reconstruction,  $\text{RSD}_i$  is a per-pixel measure of relative uncertainty in the reconstruction.

## 2.1 Covariance Functions

The choice of covariance function (i.e., kernel)  $k(\mathbf{x}, \mathbf{x}')$  encodes assumptions about object function  $f$  such as smoothness and differentiability. Therefore, it is critical that the chosen covariance function be able to capture the underlying spatial distribution of the object we are trying to reconstruct. Many popular choices for covariance functions are available in the literature [see Chapter 4 of 5, for a lucid overview]. Among them is a broad class of covariance functions, known as stationary covariance functions, that depends only on the metric distance  $r$  between any two points  $\mathbf{x}, \mathbf{x}' \in \Omega$ . Given  $\sigma_f$  as the prior variance at each location, popular stationary kernels include the squared exponential (SE) kernel

$$k_{\text{SE}}(r) = \sigma_f^2 \exp\left(-\frac{r^2}{2}\right)$$

and the Matérn kernels (MK)

$$k_{\text{MK}}(r) = \sigma_f^2 \frac{2^{1-\nu}}{\Gamma(\nu)} (\sqrt{2\nu}r)^\nu B_\nu(\sqrt{2\nu}r),$$

where  $\nu > 0$  is a constant and  $B_\nu$  is the modified Bessel function of the second kind. In the MK kernel,  $\nu$  controls the level of smoothness of  $f$ , since the order of differentiability of functions sampled from a GP with a Matérn kernel is  $\lfloor \nu \rfloor$ .  $k_{\text{SE}}$  is appropriate for describing infinitely differentiable functions, as suggested by the fact that  $\lim_{\nu \rightarrow \infty} k_{\text{MK}} = k_{\text{SE}}$  [5]. We focus on two common types of the MK kernels: MK32 (i.e.,  $\nu = 3/2$ ) and MK52 (i.e.,  $\nu = 5/2$ ).

<sup>1</sup>In principle, the components of  $\mathbf{A}$  are proportional to the intersection length, with the proportionality constant determined by beam intensity and detector efficiency. For the sake of simplicity, and without loss of generality, we set this constant to 1 here.

<sup>2</sup>We use  $\mathbb{E}[\cdot]$  to denote the expected value of a random variable.

The GP methodology offers the flexibility to use any distance metric or kernel of choice [11]. In our imaging case, we simply choose the Euclidean distance where  $r^2 = (\mathbf{x} - \mathbf{x}')^T \mathbf{\Lambda}^{-1} (\mathbf{x} - \mathbf{x}')$  and  $\mathbf{\Lambda} = l^2 \mathbf{I}$ , for any  $\mathbf{x}, \mathbf{x}' \in \Omega$ . The parameter  $l$  is referred to as the correlation length and represents the relationship between the points  $\mathbf{x}$  and  $\mathbf{x}'$ . Intuitively, a larger value of  $l$  indicates that points far away from each are strongly correlated, and vice versa. Another property of stationary kernels is that  $k(0) = \sigma_f^2$ ; hence the prior variance is constant over the domain  $\Omega$ .

These simple kernels are capable of describing objects characterized by a single length scale and range of variability, but they are not adequate for reconstructing objects with more complex variation. In order to capture variations on multiple length scales, for example, composite kernels obtained by convex superposition of two or more kernels can be used in following form,

$$k(\mathbf{x}, \mathbf{x}') = \sum_{i=1}^{N_k} \sigma_{f,i}^2 k_i(\mathbf{x}, \mathbf{x}'),$$

where the component kernel  $k_i$  can be any standard kernel, such as  $k_{\text{SE}}$  or  $k_{\text{MK}}$ , with a single correlation length parameter  $l_i$ . Additionally, when all the component kernels are stationary, we have

$$k(r) = \sum_{i=1}^{N_k} \sigma_{f,i}^2 k_i(r; l_i).$$

For notational compactness, we denote by  $\sigma_f$  the  $N_k$ -dimensional vector with components  $\sigma_{f,i}$  and denote by  $l$  the  $N_k$ -dimensional vector with components  $l_i$ . We particularly focus on homogeneous composite kernels, that is, with all component kernels of the same type. In this work  $k_i$ -s are considered to be one of  $k_{\text{SE}}$ ,  $k_{\text{MK32}}$  or  $k_{\text{MK52}}$ .

## 2.2 Hyperparameters and Optimization

The parameters associated with kernel  $k$  along with the prior constant mean  $c$  are together referred to as the hyperparameters of the reconstruction problem. The choice of hyperparameters is critical for the performance of the GP method and must be chosen judiciously. Popular parameter-tuning strategies such as leave-one-out cross-validation [12] and generalized cross-validation [13] work by “predicting” subsets of data values excluded from training. Such approaches require extensive trial and error, however, and can be computationally inefficient. Alternatively, we choose to tune hyperparameters by maximizing the marginal likelihood of  $\mathbf{y}$  [5]. Without loss of generality, we describe the hyperparameter optimization for a single kernel that can be trivially extended to composite kernel.

Given  $\mathbf{y} \sim \mathcal{N}(\mathbf{A}\mathbf{m}, \mathbf{A}\mathbf{K}\mathbf{A}^T + \Sigma_\epsilon)$  (see Eqn. (2)), the negative log-likelihood function of  $\mathbf{y}$  is

$$\mathcal{J}(c, \sigma_f, l) = \frac{1}{2} \mathbf{r}^T \mathbf{K}_y^{-1} \mathbf{r} + \frac{1}{2} \log |\mathbf{K}_y| + \frac{m}{2} \log 2\pi,$$

where  $\mathbf{r} = \mathbf{y} - \mathbf{A}\mathbf{m}$  is the residual and  $\mathbf{K}_y = \mathbf{A}\mathbf{K}\mathbf{A}^T + \Sigma_\epsilon$ . The optimal parameters  $[c^*, \sigma_f^*, l^*]$  are obtained by minimizing the following constrained optimization problem:

$$[c^*, \sigma_f^*, l^*] = \arg \min_{c, \sigma_f, l} \mathcal{J}(c, \sigma_f, l) \quad \text{s.t.} \quad \sigma_f > 0, l > 0. \quad (3)$$

Instead of explicitly solving this constrained problem, we optimize Eqn. (3) with respect to  $[c, \log(\sigma_f), \log(l)]$  (where the log applies element-wise to the components of the vectors  $\sigma_f$  and  $l$ ), which implicitly enforces the positive constraints and converts the original constrained problem to an unconstrained one. For simplicity of notation, we denote  $\boldsymbol{\beta} = [c, \log(\sigma_f), \log(l)]$  as the  $2N_k + 1$ -dimensional vector of hyperparameters.

Then we can derive the corresponding derivatives as

$$\frac{\partial \mathcal{J}}{\partial \beta_1} = \mathbf{1}^T \mathbf{A}^T \mathbf{K}_y^{-1} (\beta_1 \mathbf{A} \mathbf{1} - \mathbf{y}), \quad \text{and}$$

$$\frac{\partial \mathcal{J}}{\partial \beta_i} = \frac{1}{2} \text{tr} \left[ (\mathbf{K}_y^{-1} - \alpha \alpha^T) \frac{\partial \mathbf{K}_y}{\partial \beta_i} \right], \quad i = 2, \dots, 2N_k + 1,$$

where  $\alpha = \mathbf{K}_y^{-1}(\mathbf{y} - c\mathbf{A}\mathbf{1})$  and  $\frac{\partial \mathbf{K}_y}{\partial \beta_i}$  depends on the choice of the covariance function. Provided with these analytical derivatives, we employ a derivative-based large-scale optimization algorithm, the truncated-Newton method [3], to locate the optimal hyperparameters in Eqn. (2).

Notice that for the composite kernel with  $N_k$  basic kernels, the total number of unknown hyperparameters is  $2N_k + 1$ , since each subkernel  $k_i$  has its own prior variance  $[\sigma_f]_i$  and correlation length  $l_i$ , and in addition we have the mean

parameter  $c$ . To accelerate the optimization performance and take advantage of the nested structure between the basic kernels, we optimize the hyperparameters of the composite kernel following a sequential fashion where we gradually add one basic kernel at a time and use the optimized hyperparameters  $[\sigma_f]_i^*$  and  $l_i^*$  to initialize the optimization of  $[\sigma_f]_{i+1}$  and  $l_{i+1}$ . Initial  $c$  satisfies  $\frac{\partial \mathcal{J}}{\partial \beta_1}(c) = 0$ .

### 3 Numerical Results

We illustrate the performance of the proposed Gaussian process and compare it with the traditional optimization-based reconstruction methods. We choose two images: the standard synthetic Shepp–Logan phantom (SLP) and a real MRI image of a brain, as the ground truth objects (see Fig. 1).

Both images are discretized into  $n = 100$  pixels along each dimension. Let  $\mu_f$  and  $\sigma_f$  be the mean and standard deviation of all pixel values of the ground truth, and let  $p$  be the pixel size (see Tab. 1 for detailed values). The different choices of  $p$  intend to test the robustness of the method toward scaling differences. In general, the correlation length can be assumed to be 1 as a consequence of being scaled proportionately with the true pixel size.

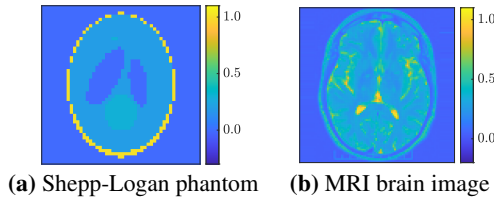


**Fig. 1:** Ground truth

Ground truth	$\mu_f$	$\sigma_f$	$p$
SLP	0.1202	0.2143	$8 \times 10^{-4}$
MRI	0.2166	0.1701	1

**Table 1:** Parameters of the ground truths

We consider the following four cases of noisy measurement  $y$  when reconstructing the object:

**Case I** The measurements are noise-free (denoted as  $\tilde{y}$ ); that is, formally the noise covariance  $\Sigma_\epsilon = 0$ . However, the resulting covariance matrix  $\mathbf{K}_y = \mathbf{A}\mathbf{K}\mathbf{A}^T$  can have a very large condition number depending on the length scale parameter  $l$  [12] and hence become numerically singular. We avoid this issue by adding a “nugget,”  $\Sigma_\epsilon = \sigma_\epsilon^2 \mathbf{I}$  with  $\sigma_\epsilon = 0.001$ , to the covariance.

**Case II** i.i.d. Gaussian noise with zero mean and standard deviation  $\sigma_\epsilon$  equal to 10% of the root-mean-square (RMS) of the noise-free measurement  $\tilde{y}$  is added to  $\tilde{y}$ , where

$$\text{RMS}(\tilde{y}) = \sqrt{\frac{1}{m} \sum_{t=1}^m \tilde{y}_t^2}, \quad \sigma_\epsilon = 0.1 \times \text{RMS}(\tilde{y}).$$

The noise model in reconstruction correctly reflects this added homoskedastic noise, so that  $\Sigma_\epsilon = \sigma_\epsilon^2 \mathbf{I}$ .

**Case III** Independent zero-mean Gaussian heteroskedastic noise is added to each measurement. The standard deviation of the noise added to  $\tilde{y}_t$  is equal to  $\alpha_t \text{RMS}(\tilde{y}_t)$ , where  $\alpha_t \sim \mathcal{U}(0.05, 0.25)$ . The noise model in reconstruction correctly reflects this added heteroskedastic noise, so that  $\sigma_{\epsilon,t} = \alpha_t \text{RMS}(\tilde{y})$  with known  $\alpha_t$ .

**Case IV** The noise is added in the same way as **Case III**; however, we assume  $\sigma_\epsilon = 0.10 \times \text{RMS}(\tilde{y})$  for reconstruction. Therefore, an imperfect description of the noise model is considered in this case.

We measure the quality of the reconstruction using the relative reconstruction error defined as

$$E_{\text{norm}} = \frac{\|\mathbf{f}_r - \mathbf{f}^*\|_F}{\|\mathbf{f}^*\|_F},$$

where  $\mathbf{f}^*$  is the ground truth and  $\mathbf{f}_r$  is the reconstruction returned by different algorithms (e.g.,  $\mathbf{m}^*$  from the proposed GP method).

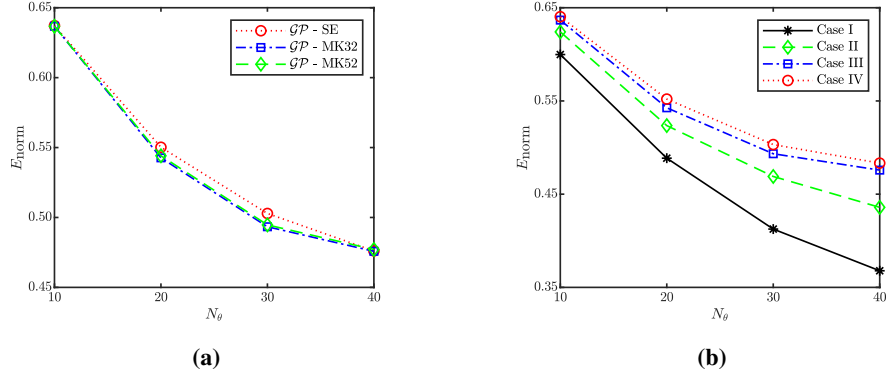


**Fig. 2:** Left 2a: Comparison of GP-based reconstruction with optimization-based techniques with varying  $N_\theta$  for Case III; right 2b: comparison of GP-based reconstruction with MK32 kernel in various test cases.

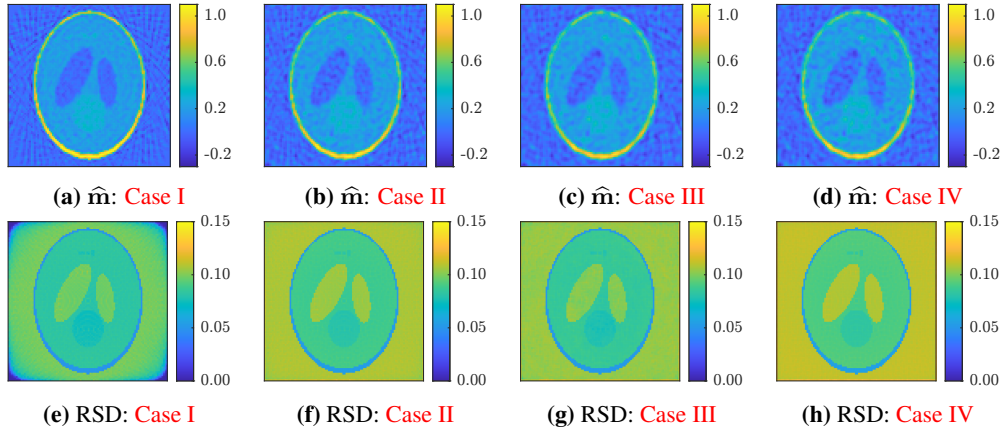


**Fig. 3:** Top: MK32-based GP reconstruction of the Shepp–Logan object with 40 angles for each case, respectively; bottom: RSD of the corresponding reconstruction.

### 3.1 Shepp–Logan Phantom

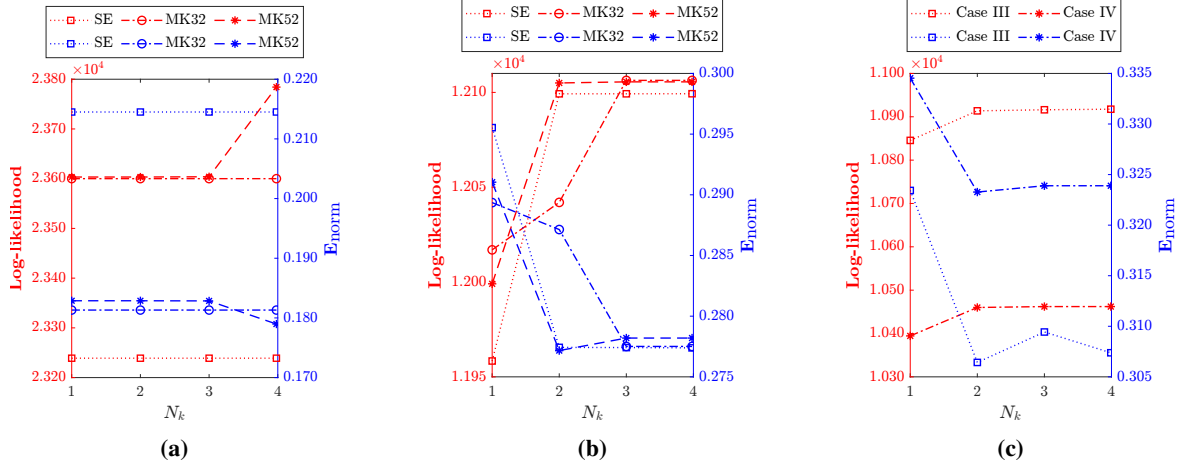
We first test single kernel-based reconstruction, namely, i.e.,  $N_k = 1$ , on the SLP object. Overall, the choice of kernel appears to have little affect on the performance of the GP method in the reconstruction of the SLP. In Fig. 2a, we compare  $E_{\text{norm}}$  using three types of kernel—SE, MK32, and MK52—for Case III. As expected, the increasing of  $N_\theta$  improves the reconstruction quality for all three kernels by providing more data. Since the MK32 kernel gives the best reconstruction (i.e., least  $E_{\text{norm}}$ ), we focus only on MK32 for further tests on SLP.

Figure 2b shows the improved reconstruction quality as  $N_\theta$  increases for all four cases; due to an increase in the number of measurements available from which the reconstruction is made. Moreover, as the noise increases from Case I to Case II,  $E_{\text{norm}}$  increases consistently for every  $N_\theta$ ; and this increase in error is most pronounced for  $N_\theta = 40$ . The reconstruction in Case IV has higher error than Case III because a homoscedastic noise model is used to reconstruct the object when the actual noise is heteroscedastic.

In Fig. 3, we visualize the reconstruction using the MK32 kernel for all four cases with  $N_\theta = 40$ . As expected, the quality of the reconstruction gradually drops as the measurement noise gets more complicated. Consistently, the corresponding RSD ( $\varepsilon = 1$ ) at any pixel increases as measurement noise becomes more complicated, indicating higher uncertainty in the reconstruction. For any reconstruction, the RSD is lower at the outer boundary of the SLP object and highest in pixels corresponding to the fine inner features of the SLP. More specifically, the uncertainties indicated by the higher RSDs are mostly noticeable at where the ground truth is 0 since the information of those regions is dominated by noise. This capability for quantitatively ascertaining the level of per-pixel reconstruction uncertainty is the biggest advantage of the GP-based approach. The returned uncertainties enable scientists to judge the reconstruction quality in the absence of ground truth. Furthermore, this capability can guide the experiment to acquire more data at the highly



uncertain/unstable region and serve as an automated engine for optimal experiment design, so that the limited resources are optimally distributed to the most needed region of interest.



**Fig. 4:** Varying log-likelihood  $\log p(\mathbf{y}|\mathbf{X})$  and  $E_{\text{norm}}$  with increasing number of various component kernels  $N_k$  for the MRI object. Left: **Case I**; middle: **Case II**; right: **Case III** and **Case IV** with MK52.

### 3.2 MRI of Brain

Now we investigate the performance of homogeneous composite kernels on a real MRI brain image. Figure 4 shows the log-likelihood values and  $E_{\text{norm}}$  using the optimized hyperparameters for different kernel types and their corresponding composites with various  $N_k$ . In **Case I**, since  $\sigma_{f,i} \sim 0 \quad \forall i = 2, 3, 4$  for both the MK32 and SE base kernels, the log-likelihood values do not increase as  $N_k$  increases. Consistently, the higher the log-likelihood value is, the better the reconstruction is based on  $E_{\text{norm}}$ . Therefore, in the absence of noise, the log-likelihood can guide the model choice in terms of kernel type. In **Case II**, the log-likelihood is approaching a constant value as  $N_k$  increases. This behavior is expected since the kernels are nested (the kernel with  $N_k$  components is a special case of kernel with more components). An increase in the complexity of the kernels does not necessarily translate to a decrease in  $E_{\text{norm}}$ , suggesting that an increase in the number of kernels can lead to an overfitting of the noisy data that in turn adversely affects the final reconstruction quality. For example, in the case of the MK52 kernel type, the log-likelihood value plateaus for  $N_k \geq 2$ , which is also the inflection point for  $E_{\text{norm}}$ .

A similar observation can be made for **Case III** and **Case IV** (see Fig. 4c). In such cases, where the kernels are nested, the optimal  $N_k$  can be chosen as soon as the log-likelihood starts to stagnate, since kernels with fewer parameters are computationally cheaper. This is akin to choosing the model with highest Akaike information criteria [14], embedded in which is Occam's razor. For the remainder of this paper, we show the results only for the MK52 component kernels because it gives the best reconstructions for the MRI object.

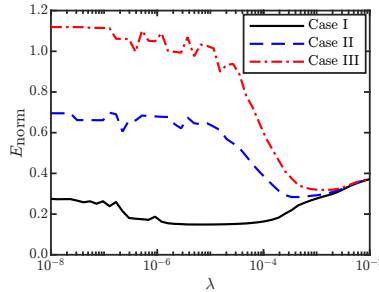


**Fig. 5:**  $E_{\text{norm}}$  for the TV-regularized reconstruction of the MRI image for various values of  $\lambda$

Next we compare the GP-based reconstruction with existing optimization-based reconstruction techniques— $\mathcal{L}_2$  reconstruction (i.e., least squares) and total variation (TV)-regularized  $\mathcal{L}_2$  reconstruction (often viewed as the state-of-the-art method) [15]. For a given set of measurements, the optimal value for the regularization parameter  $\lambda$ , denoted herein as  $\lambda^*$ , is chosen via a uniform grid search on  $\lambda \in [10^{-8}, 10^{-2}]$  corresponding to the reconstruction  $\mathbf{f}^\dagger$  that yields the

lowest value of  $E_{\text{norm}}$  (see Fig. 5). Notice that the ill-posedness of the inverse problem manifests itself in how sensitive the final reconstruction is to the regularization parameter. For example, as shown in fig. 5 **Case III**, a slight perturbation of  $\lambda$  from  $\lambda^*$  can rapidly deteriorate the reconstruction quality. Therefore, choosing the optimal regularization parameter is extremely challenging, especially in the absence of ground truth. In contrast, in the GP approach, the hyperparameters can be chosen based on more principled approaches such as maximizing the likelihood of the observed data, and the overall performance can be more systematically robust than with the regularization method.

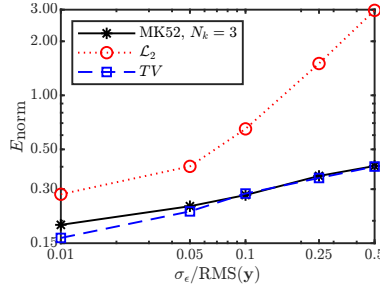


**Fig. 6:** Robustness of GP-based reconstruction using MK52 kernels method with varying noise compared with optimization-based approaches

Figure 7 shows the reconstructions obtained from various methods for Cases I–III. We can see that the GP approach outperforms the  $\mathcal{L}_2$  approach and performs comparably with TV-regularized approach (with the optimally chosen  $\lambda^*$ ). Unlike the GP approach, however, a quantifiable measure of the reconstruction uncertainty is not inherent in the optimization-based approaches. Hence, the reconstruction obtained must be accepted or rejected in totality. Moreover, in practical application when the ground truth is not available, the regularization parameter is often chosen based on heuristic approaches, such as the L-curve method, or by manual inspection of the reconstructions and using expert knowledge. In this regard, the GP method is a better option for the user with limited prior knowledge of the object.

We further compare their robustness against different levels of homoscedastic signal-to-noise ratio. In Fig. 6, the GP method outperforms the  $\mathcal{L}_2$  approach and performs similar to the TV-regularized approach. In fact, the GP method is more robust with respect to increasing level of noise, more so than the optimization-based approaches. The reason is that noise in the measurements is accounted for explicitly in deriving the GP method.

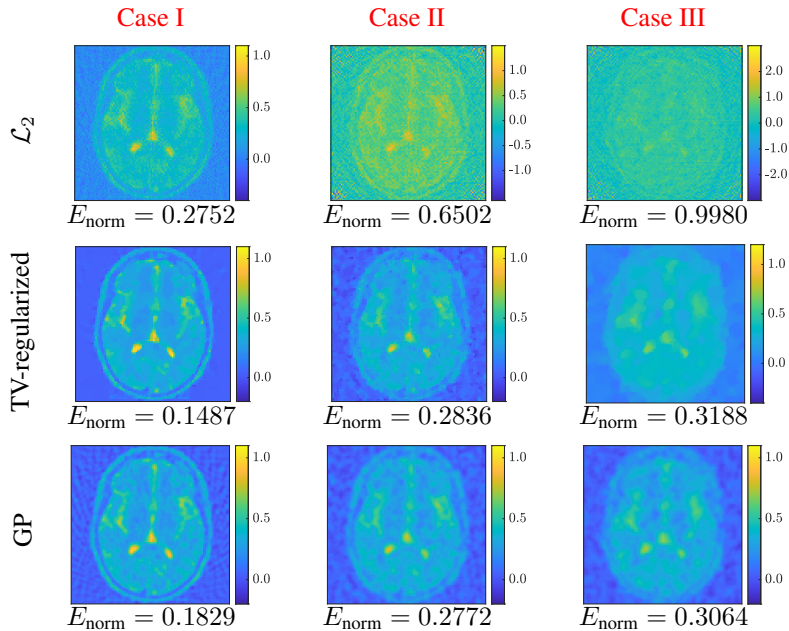


**Fig. 7:** Reconstruction comparison of the MRI image using different approaches in **Case I**, **Case II**, and **Case III**



## 4 Conclusion

Measurement and model uncertainties make the inverse problem ill-posed, inducing difficulties and inaccuracies in the search for the solution. In this letter we explore the Gaussian process to explicitly exploit the prior knowledge and provide a robust solution to the ill-posed linear inverse problem: tomographic reconstruction. Instead of providing only a point estimate of the unknown parameter, our GP-based approach provides an interval estimate with uncertainty measurements on the solution, which is extremely useful for judging the quality of the solution in the absence of ground truth. We further explore the composite kernels that are capable of capturing different length scales in the object, and we compare the performance with that of traditional optimization-based methods. Our numerical results show that, with the presence of different types of noise including both homoskedastic and heteroskedastic, that GP method greatly outperforms  $\mathcal{L}_2$  approach and achieves reconstruction comparable with the best possible results obtained by TV-based solutions, without any dependence on ground truth.

In the future, we will further explore the flexibility of GP in a real-time setting by incorporating current estimation of the object as the prior mean for the next estimation as new data comes in. This setting can be valuable for detecting in situ and time-dependent objects, an application that is closely relevant to dynamically evolving object (e.g., medical imaging). We will also address the computational efficiency of our GP approach by inducing sparsity in the covariance matrix using covariance tapering or kernels with compact support [5].

## Acknowledgments

This material was based upon work supported by the U.S. Department of Energy under contract DE-AC02-06CH11357. Agnimitra Dasgupta also acknowledges the support of the Provost Fellowship from the University of Southern California.

## References

- [1] Eric Maire and Philip John Withers. Quantitative X-ray tomography. *International Materials Reviews*, 59(1): 1–43, 2014.
- [2] Muhammad Irfan Sharif, Jian Ping Li, Javeria Naz, and Iqra Rashid. A comprehensive review on multi-organs tumor detection based on machine learning. *Pattern Recognition Letters*, 131:30–37, 2020.
- [3] Zichao Wendy Di, Si Chen, Young Pyo Hong, Chris Jacobsen, Sven Leyffer, and Stefan M Wild. Joint reconstruction of x-ray fluorescence and transmission tomography. *Optics express*, 25(12):13107–13124, 2017.
- [4] Harbir Antil, Zichao Wendy Di, and Ratna Khatri. Bilevel optimization, deep learning and fractional Laplacian regularization with applications in tomography. *Inverse Problems*, 36(6):064001, 2020.
- [5] Carl Edward Rasmussen and Christopher KI Williams. *Gaussian processes for machine learning*. Number 3. MIT press Cambridge, MA, 2006.
- [6] GY Chen and Balázs Kégl. Image denoising with complex ridgelets. *Pattern Recognition*, 40(2):578–585, 2007.
- [7] Lerenhan Li, Jinshan Pan, Wei-Sheng Lai, Changxin Gao, Nong Sang, and Ming-Hsuan Yang. Learning a discriminative prior for blind image deblurring. In *Proceedings of the IEEE Conference on Computer Vision and Pattern Recognition*, pages 6616–6625, 2018.
- [8] Dong Li, J Svensson, H Thomsen, F Medina, A Werner, and R Wolf. Bayesian soft X-ray tomography using non-stationary Gaussian processes. *Review of Scientific Instruments*, 84(8):083506, 2013.
- [9] Zenith Purisha, Carl Jidling, Niklas Wahlström, Thomas B Schön, and Simo Särkkä. Probabilistic approach to limited-data computed tomography reconstruction. *Inverse Problems*, 35(10):105004, 2019.
- [10] Gregory Beylkin. Discrete Radon transform. *IEEE transactions on acoustics, speech, and signal processing*, 35(2):162–172, 1987.
- [11] Shan Ba and V Roshan Joseph. Composite Gaussian process models for emulating expensive functions. *The Annals of Applied Statistics*, pages 1838–1860, 2012.
- [12] Shmuel Rippa. An algorithm for selecting a good value for the parameter  $c$  in radial basis function interpolation. *Advances in Computational Mathematics*, 11(2):193–210, 1999.
- [13] Hebert Montegranario and Jairo Espinosa. Radial basis functions. In *Variational regularization of 3D Data*, pages 69–81. Springer, 2014.
- [14] Hirotugu Akaike. Information theory and an extension of the maximum likelihood principle. In *Selected papers of Hirotugu Akaike*, pages 199–213. Springer, 1998.

- 
- [15] Xiang Huang, Stefan M Wild, and Zichao Wendy Di. Calibrating sensing drift in tomographic inversion. In *2019 IEEE International Conference on Image Processing (ICIP)*, pages 1267–1271. IEEE, 2019.